applied sciences

MDPI

Article

A New Methodology for Estimating Surface Albedo in Heterogeneous Areas from Satellite Imagery

Paula Andres-Anaya [1], Maria Sanchez-Aparicio [1], Susana Del Pozo [1], Susana Lagüela [1], David Hernández-López [2] and Diego Gonzalez-Aguilera [1,*]

[1] Department of Cartographic and Land Engineering, Universidad de Salamanca, Hornos Caleros, 50, 05003 Avila, Spain; paula_andana@usal.es (P.A.-A.); mar_sanchez1410@usal.es (M.S.-A.); s.p.aguilera@usal.es (S.D.P.); sulaguela@usal.es (S.L.)

[2] Institute for Regional Development (IDR), Universidad de Castilla La Mancha, Paseo de los Estudiantes, s/n, 02006 Albacete, Spain; david.hernandez@uclm.es

* Correspondence: daguilera@usal.es; Tel.: +34-920-353-505

Abstract: Precise mapping and continuous monitoring of fine-scale surface albedo are indispensable for assessing and optimizing renewable energy sources. Understanding the variations in surface reflectivity is crucial in capturing the full potential of renewable technologies, as it directly impacts the efficiency of harnessing solar energy for sustainable power generation. Satellite remote sensing stands out as the sole practical approach for estimating surface albedo at both regional and global scales. Although there are different methods to calculate albedo from satellite data, most satellite products result in low spatial resolution for large heterogeneous areas, such as urban and peri-urban areas. This paper evaluates and compares several methodologies to calculate surface albedo from Landsat 8 imagery. As a result, a new methodology for estimating surface albedo for heterogeneous areas has been proposed. The new methodology has been compared with direct and indirect albedo measurements, improving the original methodologies of Baldinelli and Silva with respect to the Arctic-Boreal Vulnerability Experiment (ABOVE) albedo images by reducing the RMSE by 85% and 52%, respectively.

Keywords: albedo; solar radiation; reflectance; satellites; remote sensing

check for updates

Citation: Andres-Anaya, P.; Sanchez-Aparicio, M.; Del Pozo, S.; Lagüela, S.; Hernández-López, D.; Gonzalez-Aguilera, D. A New Methodology for Estimating Surface Albedo in Heterogeneous Areas from Satellite Imagery. *Appl. Sci.* **2024**, *14*, 75. https://doi.org/10.3390/app14010075

Academic Editor: Maria Vicidomini

Received: 24 November 2023
Revised: 11 December 2023
Accepted: 18 December 2023
Published: 21 December 2023

Copyright: © 2023 by the authors. Licensee MDPI, Basel, Switzerland. This article is an open access article distributed under the terms and conditions of the Creative Commons Attribution (CC BY) license (https://creativecommons.org/licenses/by/4.0/).

1. Introduction

The energy transition towards networks based on renewable energies is one of the main measures for climate change mitigation. This transition is regulated by political and economic measures being established worldwide: from national regulations such as the Royal Decree-Law 244/2019 in Spain [1], which rules self-consumption and promotes renewable energies; to international accords such as the Paris Agreement [2]. The final objective of the latter is to reduce the concentration of greenhouse gases through different actions, such as the promotion of renewable energy resources, like the Sun. Currently, emphasis is given to global action plans such as the 2030 Agenda for Sustainable Development [3], whose aim is to promote the Sustainable Development Goal (SDG) number 7, of "Affordable, Reliable, Sustainable and Modern Energy for all", among 16 other goals.

The generation of affordable, reliable, sustainable, and modern energy implies the use of low-carbon energy resources, among which renewable and nuclear energy can be found. In the case of renewable energies, the use of unlimited natural resources, such as wind and solar radiation, reinforces their contribution to sustainability. Thus, the implementation of improved energy technologies towards reaching SDG 7 is boosted by the technological advances for the capture of more forms of natural resources. Among those mentioned (wind and solar radiation), the latter presents more opportunities for the improvement of its use due to its higher flexibility [4].

Global solar radiation is divided in three components [5]: direct, diffuse, and reflected radiations. The most known and used for energy applications are direct and diffuse radiation. The latter is being increasingly valued, especially in geographic areas where direct solar radiation is not abundant. An example is the region of Galicia, NW Spain, where companies are Spanish leaders in the generation of energy from diffuse solar radiation [6]. Reflected radiation is starting to be used through the installation of bifacial solar panels, although the quantification of reflected solar radiation has not been deeply studied yet [7–9]. The computation of reflected solar radiation is based on the concept of albedo, as a measure of the index of radiation that an object reflects from the total incoming radiation. For this reason, the study of the albedo is essential for the selection of the optimal photovoltaic material in bifacial panels [7], the ideal ground cover material, and the angle of inclination of the panels since the influence of albedo on solar irradiance increases with the inclination of the panels [10]. Reflected solar energy is not only used at the ground level, as it can also be used in aerial vehicles, where solar radiation reflected by the clouds increases the value of albedo due to the close position of the aerial vehicles to the clouds [11].

In addition to the energy applications, albedo is an essential parameter for different studies, such as Urban Heat Islands (UHI) [12], reduction of which is also required in the energy transition towards the reduction of the consumption of energy for air conditioning [13]. The UHI effect can be reduced thanks to the increase in the value of the surface albedo, also improving air quality within the urban area and the health of the city inhabitants, as well as reducing ambient [14] and air temperature [15]. During the last decade, several preventive measures have been implemented to reduce the UHI effect based on the concept of albedo [16,17]. Some of these measures are changes in the pavement materials for roads [18], changes in the material of the building envelopes [19], use of vegetation and green materials for roofs [20–22], and painting roofs and streets in white colour [23,24]. The objective of these measures is to increase the albedo and reflectivity of the surfaces in order to reduce absorptivity, and consequently, heat storage. This effect can also be applied to other situations where the objective is heat reduction, as in train railways, where the reduction in heat absorption leads to the reduction of railway deformation [25]. However, at a global scale, high albedo values can have an influence on global warming and climate change. An example is the case of desert areas, where the increase in reflected radiation induces an increase in latent and sensible heat fluxes and temperature and a consequent decrease in air density [26].

The multidisciplinary studies mentioned are applied in large areas, in such a way that the use of a methodology with extensive results is essential. Results at big scales can be obtained with remote sensing and satellite imagery instead of using traditional albedometers. There is a high number of space missions, satellites and Earth observation instruments that provide digital images with high quality and open access, able to provide information about the solar energy reflected by a surface, and consequently enabling the computation of albedo. Both polar [27] and geostationary [28] satellites provide products with albedo values, all with the same limitation: low spatial resolution, lower than 250 m. Other acquisition methods can provide an improvement in the spatial resolution, such as the use of Unmanned Aerial Vehicles (UAVs) [29], but these present the drawback of implying high economic cost due to the need for a specific inspection for data acquisition, in addition to the limited extension that can be covered by these platforms compared to satellites. Furthermore, the estimation of albedo from UAVs requires an accurate estimation of the Bidirectional Reflectance Distribution Function (BRDF), due to the large variation in observation angles in images acquired from UAVs.

Regarding satellite imagery that can be used for the computation of surface albedo, some of the methodologies are based on multi-angle and multi-temporal observations to take into account surface anisotropy, such as the MODIS BRDF/Albedo product [30]. The problem with this type of imagery is the poor spatial resolution, so over the years, new methodologies have been developed to obtain surface albedo data with better resolution, such as those obtained from Landsat 8 images. However, surface albedo cannot be retrieved

directly from Landsat data due to the narrow field of view of the sensor, which does not allow observing the intrinsic reflectance anisotropy of most land surfaces [31]. As a solution, different methodologies have been developed to generate surface albedo at Landsat 8 resolution (30 m) and using anisotropy information from the coarser resolution (500 m) BRDF MODIS product. There are many albedo models based on Landsat data [32–39], but none of them have been validated for their application to heterogeneous environments with vegetation and urban areas.

Taking these aspects into account, this work aims to perform a deep study of the different methodologies developed within the scientific community for the estimation of surface albedo from Landsat 8 satellite imagery (30 m spatial resolution). As a result, a new methodology has been developed for estimating surface albedo, taking into account the key aspects of all of them. In addition, this methodology can also be applied to Landsat 9 satellite imagery, provided the characteristics of the imagery sensor in this platform. The objective of the proposed methodology is to obtain a direct albedo product, increasing the spatial resolution with respect to existing products, by applying optimal calculation methodologies in heterogeneous areas. To compare the results of the new method, direct measurements of albedo from SURFRAD (SURFace RADiation budget monitoring) stations and indirect measurements of albedo from the ABOVE (Arctic-Boreal Vulnerability Experiment) space mission are used.

In summary, this paper is structured as follows: after this Introduction section, Section 2 explores the fundamental principles of the albedo concept, and Section 3 describes the use of Landsat 8, ABOVE, and SURFRAD data. Section 4 outlines the methodology proposed, while Section 5 presents the experimental results obtained after its application. Finally, Section 6 summarizes the key findings and future directions.

2. Concept of Albedo

The albedo is the coefficient of reflection of a surface and is defined as the relation between the radiation reflected on the surface and the incoming radiation. With this definition in mind, albedo and reflectance are two similar terms, but not the same. As Liang and Wang [40] state, single-wavelength albedo is the same as reflectance, but when we talk about albedo, we generally refer to a certain range of wavelengths. The wavelengths used for the computation of albedo are those of the shortwave region of the spectrum of solar light, generally between 0.25 and 3.0 μm [40]. With these, the bands of high absorption and low reflection are discarded from the process because the incoming solar radiation at the wavelength beyond 0.25–3.0 μm approaches zero. Albedo values are in the range from 0 to 1, 0 being the albedo of a black body (no reflectivity) and 1 the albedo of a white body (total reflectivity). Examples of albedo values for different surfaces on the Earth are 0.04 for vegetal coal; 0.17 for bare soil; 0.25 for green grass; 0.40 for desert sand; 0.50 for concrete; between 0.50 and 0.70 for ocean ice and glaciers; and between 0.80 and 0.90 for fresh snow [41], the latter being the highest albedo value on Earth.

There are currently two main methodologies for the computation of surface albedo: the indirect estimation from images of surface reflectance; and the direct measurement with sensors. The indirect estimation of albedo is based on the measurement of reflectance in different spectral bands from satellite or UAV platforms, and the application of methodologies to estimate albedo from the reflectance values. The direct measurement can be performed with sensors called albedometers, incorporated to meteorological stations. Both measurements are presented in this paper.

Albedo can be subclassified into different types, but according to the type of solar radiation taken into account, there are the following types:

- Black-sky albedo, also known as directional-hemispherical reflectance. Black-sky albedo is the albedo in the absence of diffuse radiation and depends on the solar zenith angle. It can be considered as the direct radiation component of the total albedo;
- White-sky albedo, also known as bi-hemispheric reflectance. White-sky albedo is the albedo for circumstances with no direct radiation and considering the diffuse

radiation as isotropic (uniform reflectance properties). It can be understood as the diffuse radiation of the total albedo;

- Blue-sky albedo: this is the surface or real albedo. There are different methodologies for its calculation from satellite observations [42], but the most commonly used methodology is the integration of the BRDF (Bidirectional Reflectance Distribution Function) through the black-sky albedo, the white-sky albedo, and the diffuse fraction of sky light. That is, blue-sky albedo is the albedo value computed under real conditions with a combination of direct and diffuse light. The computation of blue-sky albedo is the objective of this work.

The value of blue-sky albedo (hereafter called surface albedo) mainly depends on the following parameters [5,43]: the environment; the material; the point of view of the observer; the solar angle; the time of the day; the state of the sky; the geometry of the environment; and the shadows. Albedo also changes with the season: as an example, the surface can be covered by snow in winter (albedo 0.80–0.90) and with grass in spring (albedo 0.25); and changes in vegetation that happen during the year, consequently changing their surface albedo value. As an example, Zheng et al. [44] show that vegetation greenness in Inner Mongolia has a positive correlation with surface albedo from May to September (growing season), this correlation being negative the rest of the year. All these parameters of influence are considered in the methodologies that compute surface albedo through the BRDF, since this is the function that allows us to correct reflectance values and converts reflectance observations to surface albedo values. BRDF describes how the reflectance of a surface depends on the point of view of the observer and on the solar angle, and the characteristics of the surface; that is, surface reflectance depends on the view and illumination geometry, and the structure of the environment.

The BRDF correction is applied to correct in the satellite images the effects of the point of view (angle of view) and the illumination angle, in order to calculate albedo from the reflectance values of different wavelengths.

3. Materials

In order to obtain surface albedo results with good spatial resolution, this paper focuses on the use of Landsat 8 satellite data. In addition, this work uses as reference values for comparison: (1) the indirect estimations of surface albedo from satellite products generated through the ABOVE mission, and (2) the direct measurements of the Surface Radiation budget monitoring (SURFRAD) network, so that a double comparison of the results of the methodology developed is provided.

3.1. Landsat 8

Landsat is a space mission for Earth monitoring, led by NASA (Washington, DC, USA) and the United States Geological Survey (USGS) (Reston, Virginia). The last satellite launched within this program and in operation is Landsat 9 [45], which has the same technical characteristics as the previous Landsat 8, and together they present an orbit with a time lag of 8 days. Thus, the methodologies are tested and designed in this paper using Landsat 8 [37], but the work could be replicated for Landsat 9 imagery. Landsat 8 is equipped with two instruments: Operational Land Imager (OLI) (Boulder, Colorado) and Thermal InfraRed Sensor (TIRS) (Washington, DC, USA).

The computation of surface albedo requires the seven corrected reflectance bands of the OLI sensor (Table 1). These are the reflectance bands in the short-wave infrared spectrum. The other bands are discarded from the computation due to their characteristics of high absorption and low reflection of the solar radiation [32]. Depending on the surface albedo calculation methodology, coastal aerosol band 1 can be substituted for an equation of atmospheric transmittance where these aerosols are considered. Reflectance values are acquired from TOA radiance values (Landsat Collection 2 Level 1), which can be downloaded via the EarthExplorer service. Finally, these TOA radiances are transformed into BOA

reflectances, depending on the methodologies that require it. BOA reflectances (Landsat Collection 2 Level 2) may also currently be downloaded via the EarthExplorer service.

Table 1. Reflectance bands in the OLI sensor of Landsat 8 satellite used in the computation of surface albedo.

Bands	Wavelength (μm)
Band 1—Coastal aerosol	0.43–0.45
Band 2—Blue	0.45–0.51
Band 3—Green	0.53–0.59
Band 4—Red	0.64–0.67
Band 5—Near Infrared (NIR)	0.85–0.88
Band 6—Short-wave Infrared (SWIR) 1	1.57–1.65
Band 7—Short-wave Infrared (SWIR) 2	2.11–2.29

The selection of images from the Landsat 8 satellite for the computation of surface albedo has been motivated by their spatial resolution (30 m), which improves the resolution of existing surface albedo values from satellite platforms, such as the ABOVE product (500 m). Landsat 8 observations over the North of the USA were collected, in clear sky conditions (less than 10% cloud cover), during 2013, 2014, 2015, and 2016. The selection of these dates is motivated by the disposition of the ABOVE product described in the following section for the sake of comparison.

3.2. Artic-Boreal Vulnerability Experiment: ABOVE

ABOVE [46] is a campaign from the Terrestrial Ecology Program at NASA. It takes place in Alaska, West Canada, and the North of the USA.

The product for daily mean blue-sky albedo (i.e., surface albedo) is available for Northern North America (Figure 1) for the period 2000–2017 [47] on the EarthData platform. The values of surface albedo are derived from the MODIS BRDF product with 500 m resolution (MCD43 V006) [48]. The daily mean surface albedo is computed by averaging surface albedo instant values per hour, weighted by the solar radiation in each time interval. This product is used as a reference value for the evaluation of the performance of the methodologies under study in big extensions, so the dates and cloud cover meet the same conditions as for Landsat.

3.3. Surface Radiation Budget Monitoring: SURFRAD

The SURFRAD network [49] is a network of sensors that performs the monitoring of surface solar radiation in the USA.

Currently, the SURFRAD network is composed of seven stations: Montana, Colorado, Illinois, Mississippi, Pennsylvania, Nevada, and South Dakota. These areas were selected with the aim of being representative of the main climate zones in the USA. From the stations available, 4 were selected for being used in this study (Table 2), because of their coincident position within the area covered by the ABOVE mission (Figure 1). The measurements of these stations in the SURFRAD network are used as reference values for the evaluation and comparison of point values obtained by the methodologies under study for surface albedo computation. The data records from these stations can be accessed through the National Oceanic and Atmospheric Administration (NOAA) (Silver Spring, MD, USA) download platform of the USA [50].

The primary measurements in SURFRAD are solar and infrared (short-wave) radiations, regardless of whether they are upwelling or downwelling, and the complementary measurements include direct and diffuse solar radiation, Ultraviolet B (UVB), and meteorological parameters such as air temperature and atmospheric pressure.

Table 2. Information from the SURFRAD stations selected in this work: code, city, latitude, longitude, elevation, and installation date.

Code	Name	Latitude	Longitude	Elevation	Installation Date
BND	Bondville, Illinois	40.05192° N	88.37309° W	230 m	April 1994
FPK	Fort Peck, Montana	48.30783° N	105.10170° W	634 m	November 1994
PSU	Penn. State University Pennsylvania	40.72012° N	77.93085° W	376 m	June 1998
SXF	Sioux Falls, South Dakota	43.73403° N	96.62328° W	473 m	June 2003

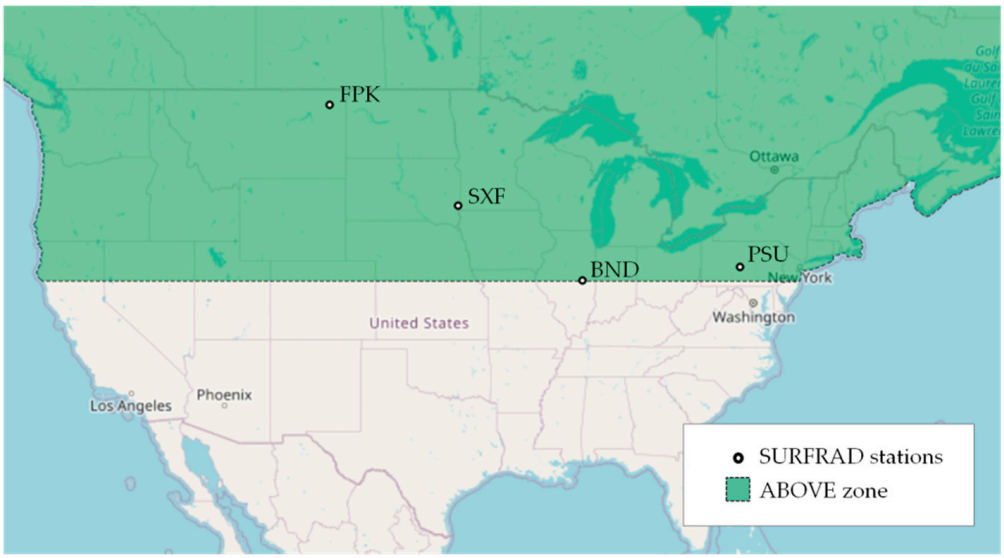


Figure 1. Location of SURFRAD stations used in this study and the area covered by the ABOVE mission.

Each station is formed by three platforms where the measurement sensors are installed. Global solar radiation is measured on the main platform with a wide-band pyranometer oriented upwards. The direct component of the radiation is measured with a pyrheliometer with normal incidence installed on an automatic solar tracker and the diffuse solar radiation is measured with a shaded pyranometer mounted on the solar tracker. Last, a third pyranometer is installed downwards on a crosshead next to the upper part of the tower, measuring radiation reflected by the surface. Data measured from direct and reflected radiation allow the computation of instant surface albedo values. The accuracies obtained for the short-wave measurements are 2% for the pyrheliometer and 5% for the pyranometer.

4. Methods

Taking into account the aforementioned methodologies for surface albedo calculation, this work has analysed four original methodologies for the computation of surface albedo with the aim of evaluating which model makes a better representation of the reality of most land covers. The difference between the four methodologies is the way the atmospheric corrections are performed: V01 and V02 correct by-product of albedo (Section 4.1) and V03 and V04 correct the Landsat 8 bands (Section 4.2) (Figure 2).

Following this evaluation, a new approach based on three combined methodologies have been tested based on the NDVI of the land cover (Section 4.4). All these methodologies are represented in Figure 2.

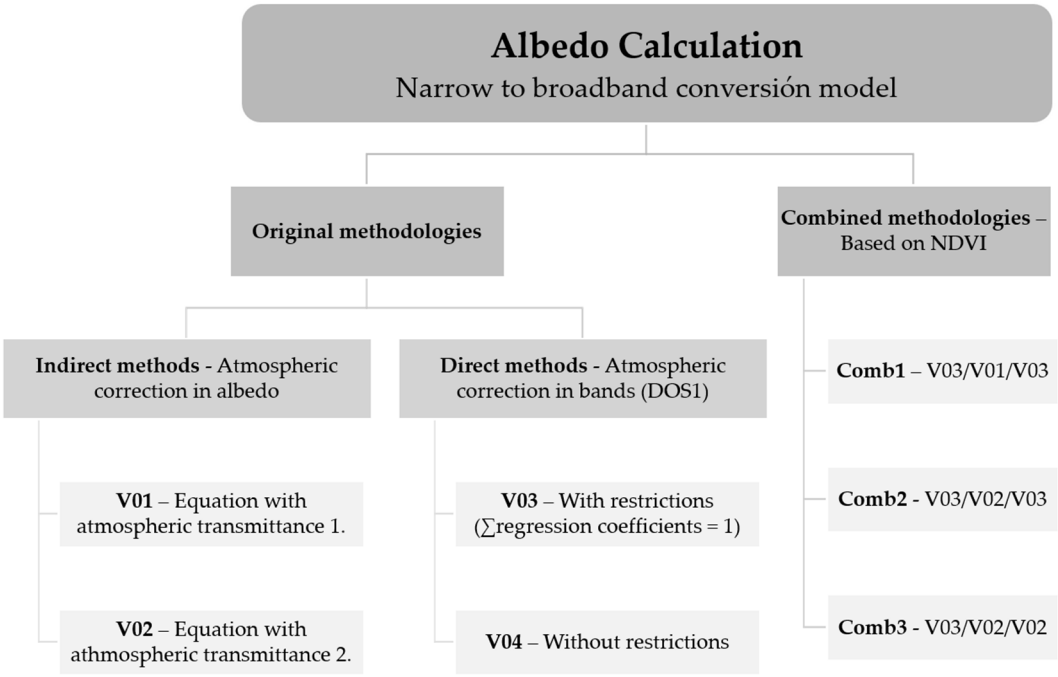


Figure 2. Methodologies used in this article for computation of surface albedo from satellite imagery. These methodologies are classified into original (existing) and combined (new methodologies). The original ones are distinguished into indirect methods from Shuai et al. 2011 [36] (V01 with atmospheric transmittance from Bastiaanssen et al. 1998 [51] and V02 with atmospheric transmittance from Chen and Ohring 1984 [52]), which perform a first surface albedo calculation and then correct it atmospherically, and direct methods from Roy et al. 2014 [31] (V03 and V04), which perform the atmospheric correction of the bands previously to the surface albedo calculation. Within these subcategories, the methodologies differ in some equations and/or parameters: V01 and V02 use different atmospheric transmittance equations and V03 and V04 use different regression coefficients. The combined methodologies use several of the above-mentioned methodologies depending on the NDVI of the ground.

4.1. Atmospheric Correction in Planetary Albedo

The surface albedo is calculated according to Equation (1) [37,51,52]:

$$\alpha = \frac{\alpha_{TOA} - \alpha_{path_radiance}}{{\tau_{SW}}^2}, \quad (1)$$

being

α: surface albedo (BOA, Bottom of Atmosphere) or albedo with atmospheric correction.
$\alpha_{path_radiance}$: atmospheric albedo.
τ_{SW}: atmospheric transmittance.
α_{TOA}: Top Of Atmosphere (TOA) albedo or planetary albedo, defined as (Equation (2)):

$$\alpha_{TOA} = \sum(\omega_\lambda \times \rho_\lambda), \quad (2)$$

where:

ω_λ: weight of each spectral band, computed as in Equation (3):

$$\omega_\lambda = \frac{ESUN_\lambda}{\sum ESUN_\lambda}, \quad (3)$$

ρ_λ: monochromatic reflectance of each spectral band (Equation (4))

$$\rho_\lambda = \frac{\pi \cdot L_\lambda \cdot d^2}{ESUN_\lambda \cdot cos\vartheta}\,, \tag{4}$$

L_λ: TOA spectral radiance ($W \cdot m^{-2} \cdot sr^{-1} \cdot \mu m^{-1}$).

$ESUN_\lambda$: mean exo-atmospheric solar spectral irradiance ($W \cdot m^{-2} \cdot sr^{-1} \cdot \mu m^{-1}$).

d: Earth-Sun distance measured in astronomical units.

ϑ: solar zenith angle in sexagesimal degrees, which corresponds to $\vartheta = 90° - \vartheta e$, where ϑe is the solar elevation.

For the case of Landsat 8 (satellite for which the equation was designed), TOA spectral radiance and mean exo-atmospheric solar spectral irradiance are defined as stated by Equations (5) and (6):

$$L_\lambda = M_L \cdot Qcal_\lambda + A_L\,, \tag{5}$$

$$ESUN_\lambda = \pi \cdot d^2 \cdot \frac{RADIANCE_{MAXIMUM_\lambda}}{REFLECTANCE_{MAXIMUM_\lambda}}\,, \tag{6}$$

Specifically:

ρ_λ: bands 2–7 from Landsat 8 are used.

M_L: Band-specific multiplicative rescaling factor, determined from the metadata.

$Q_{cal\lambda}$: quantized and calibrated standard product pixel values (DN). This value refers to each pixel in one of the bands.

A_L: Band-specific additive rescaling factor from the metadata.

$RADIANCE_{MAXIMUM\lambda}$: maximum radiance value in each band. Values are provided in the image metadata file.

$REFLECTANCE_{MAXIMUM\lambda}$: maximum reflectance value in each band. Values are provided in the image metadata file.

The value of atmospheric transmittance has yet to be defined. This value distinguishes methods denoted as V01 and V02 from one another.

It should be stated that in the case of working with Landsat 9 imagery, the TOA spectral radiance and mean exo-atmospheric solar spectral irradiance are defined by the same equations. The calibration coefficients for Equation (6) are also available in the image metadata file.

4.1.1. V01 Method

The V01 method uses an atmospheric transmission (τ_{SW}) equation in which the meteorological values are of great importance [37]. In this case, the partial pressure of water vapor is calculated taking into account the minimum air temperature, as shown in Equation (7) [53]:

$$\tau_{SW} = 0.35 + 0.627 \cdot exp\left[-\frac{0.00146 \cdot P_O}{K_t \cdot cos\vartheta} - 0.075\left(\frac{W}{cos\vartheta}\right)^{0.4}\right], \tag{7}$$

being

P_O: local atmospheric pressure (KPa).

K_t: air turbidity coefficient or clearness index. The value 1 is used for clear air, and 0.5 for extremely turbid or polluted air.

W: precipitable water (mm), computed with Equation (8):

$$W = 0.14 \cdot e_a \cdot P_O + 2.1\,, \tag{8}$$

e_a: partial pressure of atmospheric water vapor (KPa), calculated as in Equation (9):

$$e_a = 0.6108 \cdot exp\left(\frac{17.27 \cdot T_{min}}{T_{min} + 237.3}\right), \tag{9}$$

T_{min}: daily minimum air temperature from the most relevant weather station (°C).

4.1.2. V02 Method

The V02 methodology uses a completely different atmospheric transmission (τ_{SW}) equation (Equation (10)). It is calculated assuming clear sky and relatively dry conditions using a relationship based on the elevation [54]:

$$\tau_{SW} = 0.75 + 2 \times 10^{-5} \times Z_{est}\ , \quad (10)$$

being

Z_{est}: elevation above sea level from the most relevant weather station (m).

4.2. Atmospheric Correction Band to Band

Methods denoted as V03 and V04 in this work apply a direct estimation of surface albedo from the reflectivity of the BOA [55]. These methods correspond to the validated algorithms of Baldinelli et al. [32].

The estimation coefficients were calculated from empirical measurements of the surface albedo. Specifically, measurements from 16 locations on artificial urban surfaces made with a sampling time of 120 s were used. With these measurements, together with data from the OLI sensor bands (except for band 9 due to its high absorption and its low bending properties), a regression function of the least squares is generated for the correlation between surface albedo (measured in situ) and reflectivity at the BOA. This regression function was investigated with and without restrictions on the regression coefficients, whereby the methods V03 and V04 mentioned were generated. For both cases, in this work, the DOS1 atmospheric correction [56] is applied to each band used.

4.2.1. V03 Method

The V03 methodology uses the regression function with user-defined restrictions for estimating the surface albedo, α, (Equation (11)):

$$\alpha = 0.043 + 0.082{\cdot}\rho_1 + 0.064{\cdot}\rho_2 + 0.173{\cdot}\rho_3 + 0.114{\cdot}\rho_4 + 0.237{\cdot}\rho_5 + 0.252{\cdot}\rho_6 + 0.034{\cdot}\rho_7 \quad (11)$$

being

ρ_λ: monochromatic reflectance of the spectral band λ specified for Landsat 8.

Fulfilling the restrictions regarding the regression coefficients given in Equation (12):

$$\sum_{(i=0)}^{7} c_i = 1 \ and \ c_i \geq 0, \ for \ i = 1, \ldots, 7, \quad (12)$$

This restricted methodology takes into account the physics of surface albedo and provides more realistic values.

4.2.2. V04 Method

The V04 methodology given in Equation (13) uses a regression function without the restrictions of Equation (12) for estimating the surface albedo, α.

$$\alpha = 0.078 + 0.076{\cdot}\rho_1 + 0.591{\cdot}\rho_2 + 1.935{\cdot}\rho_3 - 0.492{\cdot}\rho_4 - 0.324{\cdot}\rho_5 + 1.816{\cdot}\rho_6 - 2.193{\cdot}\rho_7 \quad (13)$$

This unrestricted methodology helps to better understand the degree of correlation between predictors and surface albedo.

4.3. Evaluation and Comparison of Surface Albedo's Methods

The aim of the evaluation is to determine which of the surface albedo estimations obtained with the above methods is more accurate, through its comparison to the reference values. Two different evaluations are made for different values of reference: one evaluation taking into account the ABOVE surface albedo and another taking into account the punctual

value of the surface albedo of the SURFRAD stations. The main difference between these comparisons is that the first covers a large area with different types of land cover, while the second uses the SURFRAD value (measurement in one point position) to assess the value obtained by each methodology in a single pixel of the images. For both comparisons, satellite data from 27 dates between 2013 and 2016 at different seasons have been examined. These data are divided into 4 heterogeneous zones (FPK, BND, SXF, PSU) in which the four SURFRAD stations are located within the footprint of the ABOVE mission (Table 3).

4.3.1. Evaluation and Comparison with ABOVE

To examine Landsat images versus surface albedo ABOVE images, an algorithm is necessary for the pixel-by-pixel comparison. In this way, the value of each Landsat pixel (30 m) is compared with the value of the ABOVE pixel (500 m) where the center of the Landsat pixel falls. This comparison is made through the automation of the image processing by the Matlab® 9.3.0.713579 (R2017b) software, making a pixel-by-pixel statistical study of the Root Mean Squared Error (RMSE) between the ABOVE value and the different methodologies.

The results of the various methods examined for the same data are shown in Table 3. The results are arranged according to their mean values of the BOA Normalized Difference Vegetation Index (NDVI) [57] obtained from Equation (14) with Landsat 8 data, since this parameter has proved to have an influential role on the determination of the surface albedo [58,59].

$$NDVI = \frac{\rho_{IRC} - \rho_{RED}}{\rho_{IRC} + \rho_{RED}}, \quad (14)$$

Table 3. Data obtained from the different estimation methodologies of surface albedo with Landsat 8 (V01, V02, V03, V04) versus surface albedo ABOVE (A). Data sorted by NDVI (horizontal dashed lines). Dark green highlights the methodology with the lowest RMSE, and light green indicates the methodology with the second lowest RMSE.

Time	Code	Mean NDVI	Mean Albedo ABOVE	Pressure (KPa)	*T* min (°C)	RMSE A-V01	RMSE A-V02	RMSE A-V03	RMSE A-V04
1 November 2015	FPK	0.2141	0.2091	93.06	5.8	0.0381	0.0423	0.0268	0.1394
13 November 2015	BND	0.2464	0.1671	99.66	1.3	0.0488	0.0408	0.0453	0.1098
13 October 2014	FPK	0.2515	0.2174	94.28	0	0.0454	0.0537	0.0272	0.1212
13 August 2015	FPK	0.2785	0.1983	94.15	17.5	0.0524	0.0410	0.0517	0.1801
28 March 2015	SXF	0.3119	0.1807	96.4	−3.7	0.0751	0.0800	0.0749	0.1437
24 September 2013	FPK	0.3197	0.2038	93.92	3.8	0.0432	0.044	0.0355	0.1332
13 April 2015	SXF	0.331	0.1841	96.65	3.3	0.040	0.0434	0.0645	0.1072
8 October 2016	SXF	0.3653	0.2139	96.76	1.3	0.0729	0.0766	0.0458	0.0992
15 November 2016	BND	0.3778	0.1684	98.85	3.3	0.0689	0.0479	0.0558	0.1474
7 November 2015	SXF	0.3794	0.2076	97.24	−1.8	0.0545	0.0475	0.0403	0.1160
9 November 2016	SXF	0.3806	0.2123	97.04	−1.5	0.0530	0.0499	0.0387	0.1082
25 October 2014	BND	0.3843	0.2096	99.07	10.4	0.0646	0.0613	0.0457	0.1287
23 May 2016	BND	0.3854	0.1785	99.08	13.1	0.0523	0.0532	0.0801	0.0794
30 July 2016	FPK	0.4150	0.1796	93.68	9.3	0.0309	0.0310	0.0431	0.1463
20 April 2016	PSU	0.4364	0.1360	98.14	1.4	0.0399	0.0454	0.0794	0.1686
25 July 2014	FPK	0.4576	0.1862	93.66	10.6	0.0355	0.0359	0.0348	0.1341
26 June 2015	FPK	0.4891	0.1697	94.6	10.1	0.030	0.0309	0.0604	0.1701
8 June 2016	BND	0.5233	0.1672	99.18	11.6	0.0568	0.0595	0.0875	0.1088
23 September 2014	BND	0.5472	0.1938	100.19	8.1	0.0579	0.0601	0.0344	0.1101
14 November 2016	PSU	0.5542	0.1523	97.39	−4	0.0432	0.0436	0.0477	0.1497
4 May 2015	PSU	0.5627	0.1435	97.85	7.2	0.0446	0.0482	0.0775	0.1862
12 September 2016	BND	0.5630	0.1765	99.48	12.3	0.0460	0.0470	0.0433	0.1255
11 October 2015	PSU	0.6146	0.1595	97.17	2.4	0.0419	0.0440	0.0355	0.1246
21 October 2013	PSU	0.6209	0.1611	97.39	0.8	0.0416	0.0452	0.0338	0.1379
21 August 2016	SXF	0.7440	0.1942	96.2	10.4	0.0433	0.0449	0.0314	0.0827
12 July 2013	SXF	0.7762	0.1857	95.79	18.7	0.0250	0.0205	0.0566	0.1380
4 September 2013	BND	0.8049	0.1962	99.6	11.5	0.0396	0.0418	0.0307	0.0903
				Mean RMSE		0.0461	0.0459	0.0464	0.1262

The analysis of the results collected in Table 3 and the RMSE values for each methodology has made possible the determination of the V03 methodology as the one that responds better (RMSE with the lowest value) for NDVI $\geq$ 0.563 and NDVI $\leq$ 0.385, while the V01 method shows the best results for NDVI > 0.385 and NDVI < 0.563.

4.3.2. Evaluation and Comparison with SURFRAD

The surface albedo of the SURFRAD stations is calculated thanks to the pyranometer at the highest position in each platform (about 10 m). In this way, the surface albedo value measured is representative of a circular footprint, of approximately 60 m radius [60], the size of which varies depending on the height of the tower where the instrument is located [61].

In order to use the surface albedo data from SURFRAD stations for comparison, the heterogeneity of the land cover has to be investigated. Four different geostatistical attributes are used for this purpose: the relative coefficient of variation (RCV), the index of scale requirements (RSE), the relative strength of spatial correlation (RST), and the relative proportion of structural variation (RSV). RCV is a useful measure of the relative dispersion of the data and provides an estimate of the overall variability, and hence heterogeneity, of the data, regardless of spatial scale. RSE examines the range of variograms using two spatial thresholds with respect to the true spatial extent of a given measurement site. RST provides a spatially explicit representation of where the most different sources of surface albedo variability are likely to be found. RSV is used to assess the importance of spatial structure in the total variability of the data.

The four geostatistical attributes are combined into an equation, resulting in the ST_{SCORE} (Equation (15)), which represents a spatial representativeness rating. If the spherical variogram model does not provide a good fit, another indicator, the RAW_{SCORE} (Equation (16)), can be used to provide a new spatial representativeness score. Both ratings are directly proportional to the representativeness of the location, and the zones are considered heterogeneous or with large land cover differences if both ratings have a value below 2.

$$ST_{SCORE} = \left(\frac{|R_{CV}| + |R_{ST}| + |R_{SV}|}{3} + R_{SE} \right)^{-1}, \quad (15)$$

$$RAW_{SCORE} = |2R_{CV}|^{-1}, \quad (16)$$

Table 4 shows the results of Sánchez-Zapero et al. [59], which correspond to the SURFRAD stations selected for this project. The ratings show that the surroundings of the FPK and PSU stations are not always homogeneous since in these stations both ST_{SCORE} and RAW_{SCORE} are below 2 either in the leaf-off or in the leaf-on period.

Table 4. Characteristics of the SURFRAD sites providing data during the 2014–2018 period. In bold are highlighted ST_{score} and RAW_{score}, where both have values less than 2 and are therefore considered heterogeneous areas.

Code	Footprint (m)	Season Period	RCV(%)	RSE(%)	RST(%)	RSV(%)	ST_{SCORE}	RAW_{SCORE}
BND	126	Leaf-off	5.24	42.63	−5.17	59.16	1.52	9.54
		Leaf-on	−4.56	48.50	2.84	37.10	1.58	10.9
FPK	126	Leaf-off	7.01	19.5	−2.03	−1.25	4.37	7.13
		Leaf-on	42.27	23.5	3.36	69.44	**1.62**	**1.18**
PSU	126	Leaf-off	66.21	24.94	12.73	61.96	**1.39**	**0.76**
		Leaf-on	5.06	22.86	3.16	−14.45	3.29	9.89
SXF	32	Leaf-off	7.33	75.5	1.56	−6.74	1.24	6.82
		Leaf-on	21.08	49.5	7.29	104.41	1.07	2.37

Based on these data, Penn. State Univ., Pennsylvania (PSU) should not be used to assess the accuracy during the leafless season, and Fort Peck, Montana (FPK) should be discarded during the leaf season. These values represent the reality of the surroundings of the SURFRAD stations, so if the surrounding is heterogeneous, the ABOVE value cannot be compared to the SURFRAD data because of the presence of different vegetation cover in the pixel footprint and therefore a contaminated result.

An additional investigation of the heterogeneity of the land cover of the data selected for this project was carried out via the NDVI calculated from Landsat 8 current images. Finally, it was concluded that the PSU has a heterogeneous environment (Figure 3), so the conclusions of Table 4 are correct. On the contrary, it is found that the rest of the stations have a homogeneous environment; therefore, it is shown that the data from the FPK station can be used for seasonal periods with both leaves and no leaves. Therefore, the FPK station is used when examining the point comparison with SURFRAD data, and the PSU station is discarded.

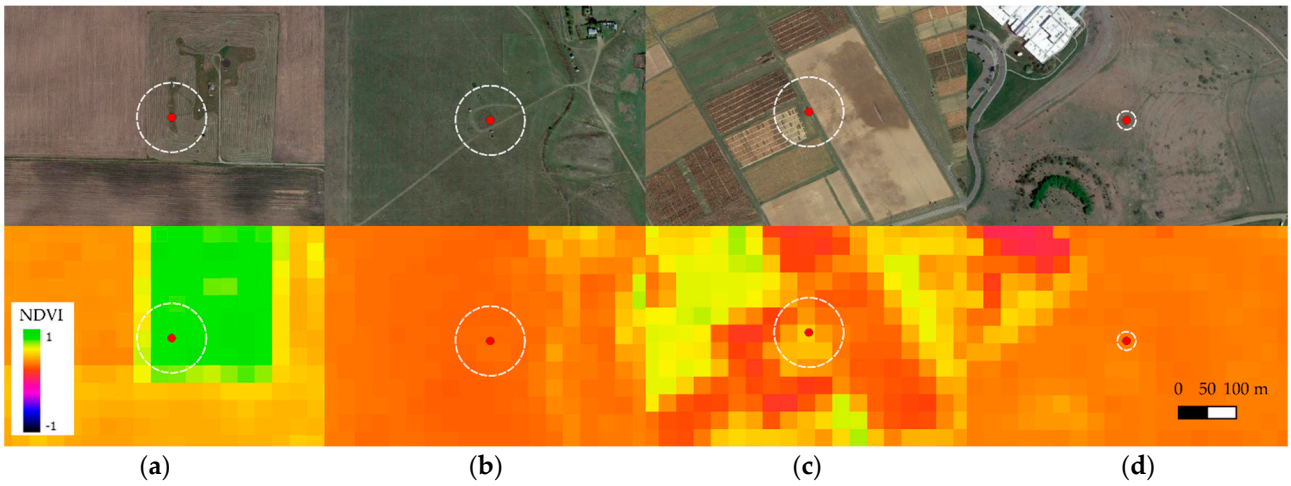


Figure 3. RGB display of Google Satellite vs NDVI of Landsat 8 from SURFRAD (**a**) BND, (**b**) FPK, (**c**) PSU, and (**d**) SXF stations. The circle at each station corresponds to the albedometer footprint. The image has North orientation (the top of the image is oriented to the North).

Taking into account the recommendations on the homogeneity of the land cover of the SURFRAD stations to compare with satellite data, five of the case studies of the PSU station for seasonal periods without leaves were discarded. In view of this, the results of the V02 methodology were closer to the surface albedo data of the SURFRAD station in 91% of the study cases, regardless of the value of the NDVI. The second-best results were achieved with the V01 methodology. Methodologies V03 and V04 provided the worst results in all of their cases, despite being methodologies based on albedometers similar to those of the SURFRAD network. This may be due to the fact that these methodologies were developed empirically from urban observations (asphalt, concrete, etc.) at static stations, as opposed to SURFRAD stations which obtain observations from rural areas (pasture, crops, etc.).

The results of the various existing methods for surface albedo computation examined with Landsat 8 images compared to the measurements of the corresponding SURFRAD stations for the same date were as follows (Table 5).

Table 5. Results of the comparison with specific data from SURFRAD stations (S) and the different methodologies with Landsat 8 images (V01, V02, V03, V04). Data ordered and separated by NDVI: NDVI $\leq$ 0.385; 0.385 > NDVI > 0.563; NDVI $\geq$ 0.563 (horizontal dashed lines).

Time	Code	NDVI	Albedo SURFRAD	Albedo ABOVE	Difference SURFRAD—ABOVE	Difference SURFRAD—V01	Difference SURFRAD—V02	Difference SURFRAD—V03	Difference SURFRAD—V04
8 June 2016	BND	0.2444	0.1241	0.164	−0.0398	−0.0823	−0.0676	−0.1042	−0.2288
25 October 2014	BND	0.2790	0.0786	0.184	−0.1053	−0.1320	−0.0928	−0.1333	−0.2726
13 November 2015	BND	0.2919	0.1250	0.149	−0.0239	−0.0575	−0.0586	−0.1026	−0.2209
4 September 2013	BND	0.294	0.1120	0.163	−0.0509	−0.0534	−0.0532	−0.1013	−0.2135
1 November 2015	FPK	0.3041	0.1214	0.167	−0.0455	−0.0448	−0.0438	−0.0897	−0.2093
30 July 2016	FPK	0.3216	0.1394	0.192	−0.0525	−0.0549	−0.0591	−0.0959	−0.2185
25 July 2014	FPK	0.3732	0.0940	0.2	−0.1059	−0.0887	−0.0726	−0.1170	−0.2483
24 September 2013	FPK	0.4169	0.1031	0.177	−0.0738	−0.0548	−0.0465	−0.0941	−0.2250
28 March 2015	SXF	0.4470	0.1036	0.184	−0.0803	−0.0454	−0.0394	−0.0938	−0.2355
7 November 2015	SXF	0.4727	0.0940	0.22	−0.1259	−0.0920	−0.0693	−0.1143	−0.2642
15 November 2016	BND	0.4990	0.1376	0.162	−0.0243	−0.0952	−0.0647	−0.1031	−0.2031
9 November 2016	SXF	0.4999	0.0948	0.212	−0.1171	−0.0842	−0.0641	−0.1080	−0.2575
12 September 2016	BND	0.5059	0.1183	0.15	−0.03162	−0.0996	−0.0796	−0.1151	−0.2013
12 July 2013	SXF	0.5608	0.1231	0.185	−0.0618	−0.0066	−0.0049	−0.0666	−0.2014
26 June 2015	FPK	0.5631	0.1566	0.179	−0.0223	−0.0254	−0.0180	−0.0796	−0.2079
23 September 2014	BND	0.5685	0.1388	0.146	−0.0071	−0.0257	−0.0205	−0.0698	−0.1628
13 October 2014	FPK	0.5940	0.1265	0.176	−0.0494	−0.0411	−0.0331	−0.0773	−0.1812
23 May 2016	BND	0.5941	0.1196	0.167	−0.0473	−0.0836	−0.0603	−0.1059	−0.2111
13 August 2015	FPK	0.6744	0.1566	0.181	−0.0243	−0.0174	−0.0099	−0.0577	−0.2197
13 April 2015	SXF	0.7071	0.1474	0.206	−0.0585	−0.0242	−0.0201	−0.0779	−0.1990
21 August 2016	SXF	0.8244	0.1348	0.227	−0.0921	−0.0626	−0.0399	−0.0909	−0.2128
8 October 2016	SXF	0.8836	0.1606	0.203	−0.0423	−0.0205	−0.0148	−0.0724	−0.1413

4.4. Proposed Method for Estimating Surface Albedo

According to the values shown in Table 3, in ascending order of their NDVI value, the two methodologies that result in values closer to the ABOVE values (and consequently considered as more accurate) are V01 for intermediate NDVI values (0.385 > NDVI > 0.563) and V03 for high (NDVI $\geq$ 0.563) and low (NDVI $\leq$ 0.385) NDVI values. If only ABOVE values were used as for comparison and validation, the conclusion would be to use methodologies V01 and V03 for a new combined methodology, where the NDVI value of each pixel determines the application of one methodology or the other.

The same dates and locations used for the comparison with ABOVE were subjected to a study of punctual values for pixels coincident with the position of four SURFRAD stations. The results included in Table 5 have shown that the methodology that computes surface albedo values closest to the values measured in the SURFRAD stations is methodology V02, for all NDVI values. In this comparison, the fact that all surfaces considered present low vegetation, means NDVI values between 0.20 and 0.50 (Figure 3) must be taken into account, because this comparison with data from SURFRAD stations does not include urban areas or areas with high vegetation.

Given the results obtained by both comparisons (ABOVE and SURFRAD), three new methodologies are designed and tested in this work, all of them based on the combination of more than one existing method, using the NDVI value of each pixel as an indicator of the existing surface albedo method to apply (Table 6). In this way, the combined methodology is adaptative to the type of land cover as a function of its NDVI value [62]. The first combined methodology proposed uses the V03 methodology for NDVI values below 0.20 (corresponding to urban areas) and over 0.50 (associated to high vegetation); and the V01 methodology for intermediate NDVI values (low vegetation). The second combined methodology proposed is based on the same principle as the first, using the V02 methodology instead of V01 for intermediate NDVI values. In this way, the second combined methodology incorporates the results from the punctual comparisons with data from SURFRAD stations. The third combined methodology also joins the results from the comparisons with ABOVE and SURFRAD, respectively, using only one inflexion value for NDVI values, taking into account that the V03 methodology was originally designed to be implemented in urban areas (NDVI below 0.20) [32]. Thus, V03 and V02 methodologies are applied if the NDVI of each pixel is below or over 0.20, respectively.

Table 6. Combined methodologies proposed, with their criteria for NDVI Evaluation per pixel.

Classes	NDVI	Combined 1	Combined 2	Combined 3
Urban Areas	[−1.00–0.20)	V03	V03	V03
Low Vegetation	[0.20–0.50]	V01	V02	V02
High Vegetation	(0.50–1.00]	V03	V03	V02

In this way, the combined methodologies proposed conform an adaptative methodology for the estimation of surface albedo in each pixel based on the NDVI, providing more accurate data for mapping and monitoring the surface albedo.

5. Experimental Results

5.1. Quantitative Evaluation

The surface albedo results obtained by the three combined strategies are compared to the ABOVE product, which is considered as a reference. This comparison is made through the automation of the image processing by the Matlab® 9.3.0.713579 (R2017b) software. The areas and data selected to validate the various strategies combined were the same as in the previous sections. The results of the comparisons are shown in Table 7.

Table 7. Comparative results between surface albedo ABOVE (A) data and combined methods (Comb1, Comb2, Comb3). The best methodologies for each case study are highlighted in dark green. The second-best methodology is emphasized in light green. The results that have improved with the combined methods with respect to the application of a single methodology are in bold.

Date	Code	RMSE A-Comb1	RMSE A-Comb2	RMSE A-Comb3
1 November 2015	FPK	0.0309	0.0377	0.0377
13 November 2015	BND	0.0461	0.0405	**0.0396**
13 October 2014	FPK	0.0442	0.0533	0.0535
13 August 2015	FPK	0.0512	0.0429	0.0428
28 March 2015	SXF	**0.0607**	0.0643	**0.0642**
24 September 2013	FPK	0.0419	0.0436	0.0451
13 April 2015	SXF	**0.0409**	0.0437	**0.0425**
8 October 2016	SXF	0.0696	0.0727	0.0759
15 November 2016	BND	0.0647	0.0461	**0.0447**
7 November 2015	SXF	0.0530	0.0439	0.0470
9 November 2016	SXF	0.0512	0.0457	0.0494
25 October 2014	BND	0.0602	0.0562	0.0596
23 May 2016	BND	0.0537	0.0545	**0.0515**
30 July 2016	FPK	0.0333	0.0333	0.0324
20 April 2016	PSU	0.0515	0.0546	**0.0445**
25 July 2014	FPK	**0.0299**	0.0361	0.0360
26 June 2015	FPK	0.0431	0.0435	0.0312
8 June 2016	BND	0.0696	0.0713	**0.0560**
23 September 2014	BND	0.0521	0.0534	0.0585
14 November 2016	PSU	0.0490	0.0482	**0.0429**
4 May 2015	PSU	0.0700	0.0714	**0.0464**
12 September 2016	BND	0.0531	0.0544	0.0443
11 October 2015	PSU	0.0374	0.0377	0.0430
21 October 2013	PSU	0.0364	0.0368	0.0445
21 August 2016	SXF	**0.0312**	**0.0312**	0.0440
12 July 2013	SXF	0.0564	0.0562	**0.0197**
4 September 2013	BND	0.0310	0.0307	0.0399
Mean RMSE		0.0470	0.0469	**0.0445**

The results of Table 7 show that the combined methods 1 and 2 (Comb1 and Comb2) present very similar results. These results were expected due to the similarity between methods V01 and V02 (Table 6). On the other hand, the combined methodology 3 (Comb3) improves the results of methodologies V01 and V02, decreasing the RMSE in 85% of the cases, while improving it in 52% of the cases with respect to the use of the methodology V03.

In general, combined method 3 (Comb3) gives better results than combined methods 1 and 2 (Comb1 and Comb2) and improves the outcome of both in 45% of the cases.

Similarly, and taking into account the results of Tables 5 and 7, it is verified that the combined methodology 3 (Comb3) is the methodology that improves the results of the original methodologies V01, V02, and V03, having the lowest mean RMSE of all the cases studied, with a value of 0.0445.

5.2. Visual Evaluation

Visual assessment is a fundamental procedure when analysing the results of satellite imagery. In this way, it is possible to evaluate areas where there is a greater difference in surface albedo with respect to the ABOVE reference images. This visual comparison is made using the QGIS® Geographic Information System.

Figure 4 shows one of the dates selected for the study in the Illinois area, where the SURFRAD BND station is located. This workspace is characterized by the presence of a large urban core: Champaign. In Figure 4, the conclusions in the quantitative assessment section are visually checked. On the one hand, the V03 (Figure 4f) method works better in urban areas (NDVI values below 0.20), while the V01 (Figure 4d) and V02 (Figure 4e) methods generally work better in the non-urban areas (NDVI values over 0.20). On the other hand, the combined method 3 (Figure 4i) gives better results than the combined methods 1 (Figure 4g) and 2 (Figure 4h). As shown in Figure 5, the combined methodology 3 (Comb3) gets 3 scores very similar to the V01 and V02 methodology but improves the results in urban areas like the V03 methodology.

This improvement in the results of combined methodology 3 (Comb3) in urban areas is due to the use of the adequate existing method for the adequate pixels, such as the application of the V03 methodology only for NDVI values below 0.20. This difference in results can be seen in Figure 5, which shows in more detail the difference in surface albedo values in the center of the town of Champaign between the V02 methodology (similar to V01) and V03.

This visual assessment allows us to confirm the conclusions of the quantitative assessment and to show again that the combined methodology 3 (Comb3) offers improvements over the original methods and the remaining combined methods.

In addition, as shown in the ABOVE surface albedo image in Figure 4b, the difference in spatial resolution between the reference image and the output images is visually shown, creating a mixture of surface albedo since the resolution of the pixels is greater than the surface elements. The situation is similar with other types of satellite imagery, such as those of the Earth surface temperature [63], so the range of some errors is understandable, especially in urban areas due to the heterogeneity of the surfaces.

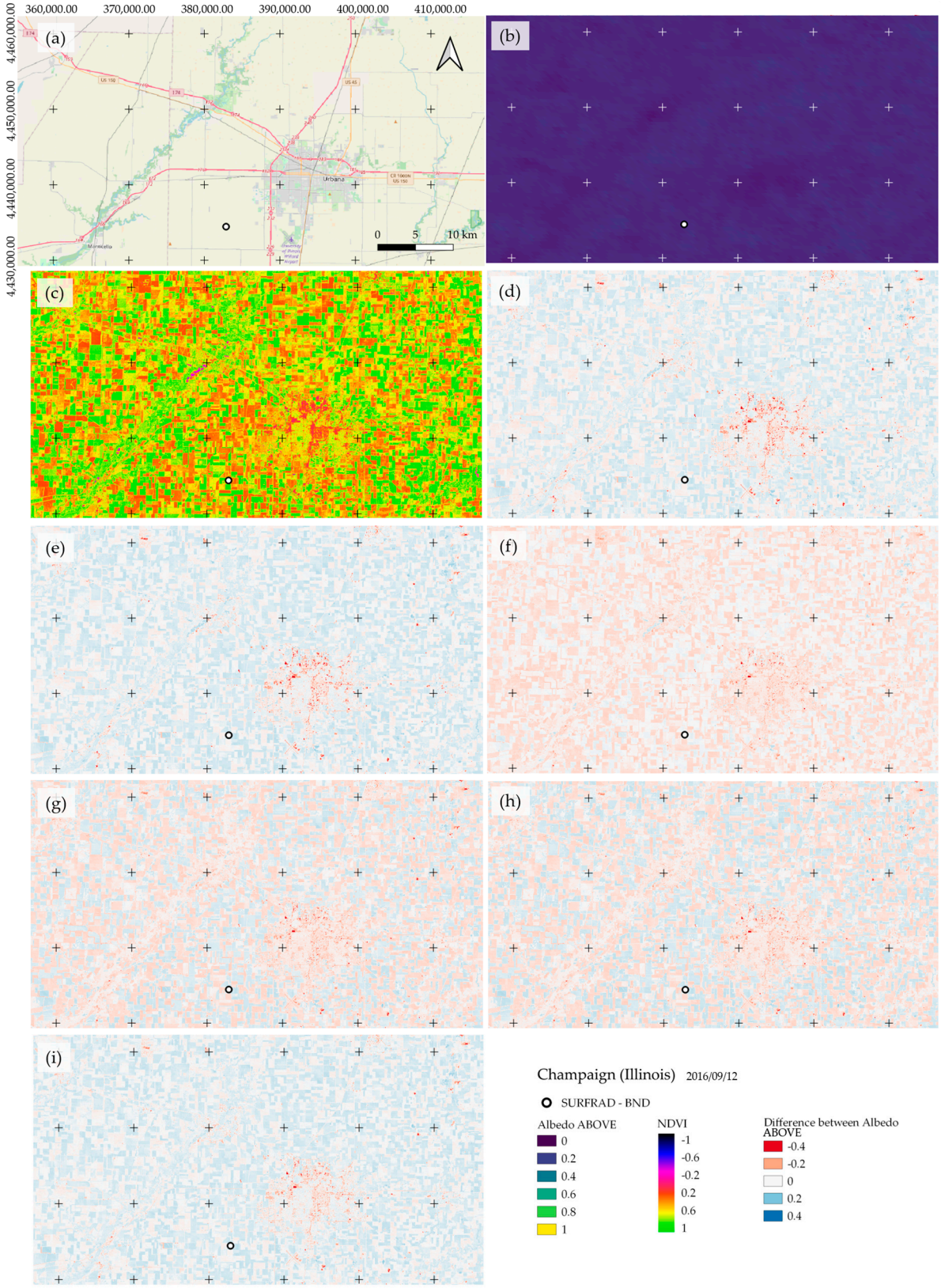


Figure 4. 12 September 2016 Visual Assessment of Illinois Area: (**a**) Open Street Map of the area under study; (**b**) ABOVE surface albedo; (**c**) NDVI; difference between ABOVE surface albedo and (**d**) V01 (**e**) V02 (**f**) V03 (**g**) Comb1 (**h**) Comb2 (**i**) Comb3 methods. Figure (**a**) shows the North orientation, scale, and coordinates for all images.

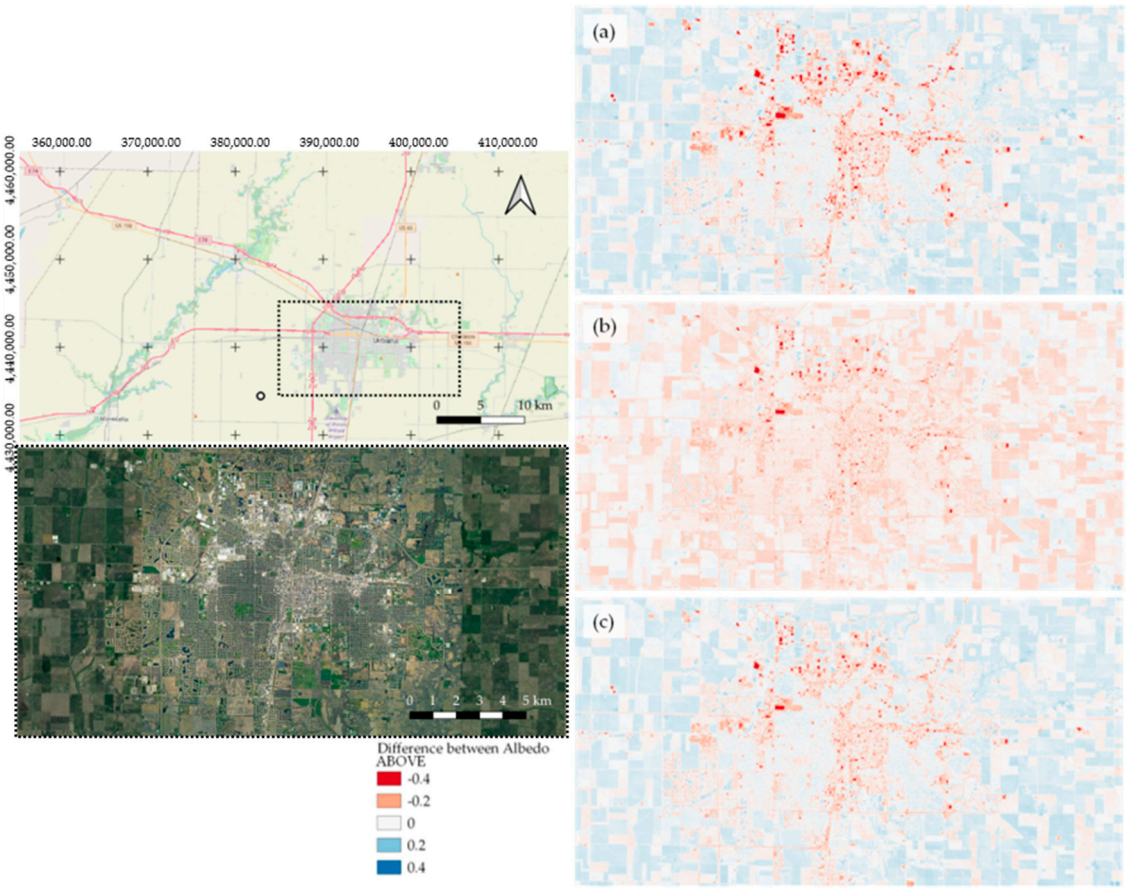


Figure 5. Visual evaluation of the surface albedo difference of the city of Champaign on 12 September 2016, between ABOVE and the different methodologies: (**a**) V02, (**b**) V03, and (**c**) Comb3. Graphical scale and colour palette corresponding to the difference between surface albedo ABOVE from Figure 4. North, coordinates, and scale are shown in the images from OpenStreetMap at the (**left**).

6. Conclusions

The need to measure surface albedo at a global scale in different land cover types, with an improved spatial resolution regarding current existing satellite surface albedo products, is the main motivation for the methodology developed in this work. The combined methodologies using Landsat 8 or Landsat 9 imagery (resolution 30 m) were designed after the analysis and comparison of four existing methodologies regarding ABOVE surface albedo imagery (resolution 500 m) and punctual surface albedo values measured in SURFRAD stations.

The analysis based on ABOVE imagery shows that the surface albedo obtained with methodology V01 in pixels with intermediate NDVI values between 0.20 and 0.50 (low vegetation) are the best values, although the V02 methodology generates close results. Methodology V03 generates the best results of surface albedo for pixels with NDVI values below 0.20 (urban areas). The three methodologies had a good performance in surface albedo computation for pixels with NDVI values over 0.5 (high vegetation), although methodology V03 performs slightly better.

The evaluation considering SURFRAD punctual values shows that the most accurate methodology is V02, regardless of the NDVI value of the pixel. Provided that all SURFRAD stations are located in areas with low vegetation, these results are coherent with the results obtained after the analysis with ABOVE imagery. However, this result reinforces the application of the V02 methodology in pixels with intermediate NDVI values between 0.20 and 0.50.

In this way, three different combined methodologies were developed, consisting of different combinations of the existing methodologies V01, V02, and V03 applied to different pixel NDVI values.

A final comparison with ABOVE images shows that the combined methodology 3 (Comb3) is the optimal combined methodology. Combined methodology 3 applies the V02 methodology to pixels with NDVI values over 0.20 and the V03 methodology for the other, and results in an RMSE constant for most types of terrestrial coverage, which is improved regarding the individual methodologies: combined methodology 3 is 85% better than methodology V02 and 52% better than the V03 methodology, when applied to heterogeneous areas (mixing urban and vegetation land uses) and considering the similarity to the ABOVE product as an improvement. A visual evaluation also shows the best results for combined methodology 3.

Future research lines will deal with the combination of surface albedo and Land Surface Temperature satellite data towards the determination of the reflected and direct components of the incoming solar radiation, with application to UHI and solar energy quantification [9,64]. To improve these future lines, it is worth highlighting the spatial-temporal resolution limitations of the proposed methodology, which could be solved and complemented with additional data provided with drones if the study required it.

Furthermore, to address the spatial resolution constraints, exploration into alternative satellite missions becomes imperative. Integration of datasets from high-performance satellite platforms like Sentinel-2, boasting a resolution of 10 m for NDVI, or even Very High Resolution (VHR) platforms such as Planet with an approximate 3-m GSD for NDVI, could significantly enhance the BRDF estimation, subsequently refining the accuracy of surface albedo determination.

In addition, the evaluation of the methodology and its refinement could benefit from the determination of RMSE for areas with very low NDVI values (below 0.2). This action will imply the establishment of pyranometers in complementary locations to the official networks.

Author Contributions: Conceptualization, P.A.-A. and S.L.; methodology, P.A.-A., S.L., S.D.P., M.S.-A., D.H.-L. and D.G.-A.; software, P.A.-A.; validation, P.A.-A., S.D.P. and S.L.; formal analysis, M.S.-A.; investigation, D.H.-L., D.G.-A. and M.S.-A.; resources, P.A.-A., D.H.-L. and D.G.-A.; data curation, M.S.-A.; writing—original draft preparation, P.A.-A.; writing—review and editing, D.H-L., D.G.-A., M.S.-A. and S.D.P.; visualization, S.D.P.; supervision, S.L., D.H.-L. and D.G.-A.; project administration, S.L.; funding acquisition, S.L. All authors have read and agreed to the published version of the manuscript.

Funding: This research was funded by Cátedra Iberdrola VIII Centenary of the University of Salamanca; the Junta de Castilla y León with the Fondo Social Europeo through programs for human resources (grant number EDU/601/2020); and the Ministry of Education, Culture and Sports (Government of Spain) through human resources (grant number FPU19/06034). The University of Salamanca acknowledges the TREEADS project, which has received funding from the European Union's Horizon 2020 research and innovation programme under grant agreement No. 101036926. Content reflects only the author's view and the European Commission is not responsible for any use that may be made of the information it contains.

Institutional Review Board Statement: Not applicable.

Informed Consent Statement: Not applicable.

Data Availability Statement: Publicly available datasets were analyzed in this study. This data can be found here: SURFRAD data [https://gml.noaa.gov/dv/data/index.php?category=Radiation&parameter_name=Surface+Radiation], Landsat data [https://earthexplorer.usgs.gov/] and ABOVE data [https://search.earthdata.nasa.gov/search/granules?p=C2113058037-ORNL_CLOUD&pg[0][v]=f&pg[0][gsk]=-start_date&fpj=ABoVE&as[project][0]=ABoVE&tl=1703002974.863!3!!&lat=56.366111904614044&long=-172.6875] (all accessed on 17 December 2023).

Acknowledgments: The authors want to thank the Spanish Ministry of Education, Culture and Sports for providing an FPU grant (Training Program for Academic Staff) to the corresponding author of this paper. The same acknowledgement is given to Junta de Castilla y León. Authors would like to thank Iberdrola España SAU and University of Salamanca for their support in human and material resources given through Cátedra Iberdrola VIII Centenario.

Conflicts of Interest: The authors declare no conflict of interest.

References

1. BOE 2019. Real Decreto 244/2019, de 5 de Abril, por el que se Regulan las Condiciones Administrativas, Técnicas y Económicas del Autoconsumo de Energía Eléctrica. Actualidad Jurídica Ambiental, (90); pp. 68–71. Available online: https://www.boe.es/eli/es/rd/2019/04/05/244 (accessed on 17 December 2023).
2. Paris Agreement 2015. Conference of the Parties Twenty First Session. Paris, 30 November to 11 December 2015. Available online: https://unfccc.int/sites/default/files/resource/docs/2015/cop21/eng/l09r01.pdf (accessed on 17 December 2023).
3. United Nations General Assembly 2015. Resolution 70/1. Transforming Our World: The 2030 Agenda for Sustainable Development. A/RES/70/1. October 2015. Available online: https://unctad.org/system/files/official-document/ares70d1_en.pdf (accessed on 17 December 2023).
4. Rinsel, S.R.; Riemke, R.L.; Hoffman, V.H. Challenges and solution technologies for the integration of variable renewable energy sources—A review. *Renew. Energy* **2020**, *145*, 2271–2285.
5. Scharmer, K. *The European Solar Radiation Atlas: Fundamentals and Maps*; Presses Des MINES: Paris, France, 2000; Volume 1.
6. Cope. Desmontando Mitos: Galicia, Líder en España en Autoconsumo de Energía Solar. Cope Galicia, Entrevista a Fernando Romero, Director General de EDF-Solar. Available online: https://www.cope.es/emisoras/galicia/a-coruna-provincia/santiago/noticias/hace-falta-radiacion-directa-para-generar-energia-solar-20200122_599837 (accessed on 17 December 2023).
7. Brennan, M.P.; Abramase, A.L.; Andrews, R.W.; Pearce, J.M. Effects of spectral albedo on solar photovoltaic devices. *Sol. Energy Mater. Sol. Cells* **2014**, *124*, 111–116. [CrossRef]
8. Ricco Galluzzo, F.; Zani, P.E.; Foti, M.; Canino, A.; Gerardi, C.; Lombardo, S. Numerical modeling of bifacial PV string performance: Perimeter effect and influence of uniaxial solar trackers. *Energies* **2020**, *13*, 869. [CrossRef]
9. Raina, G.; Sinha, S. A simulation study to evaluate and compare monofacial Vs bifacial PERC PV cells and the effect of albedo on bifacial performance. *Mater. Today Proc.* **2021**, *46*, 5242–5247. [CrossRef]
10. Mubarak, R.; Hofmann, M.; Riechelmann, S.; Seckmeyer, G. Comparison of modelled and measured tilted solar irradiance for photovoltaic applications. *Energies* **2017**, *10*, 1688. [CrossRef]
11. Smith, T.; Trancossi, M.; Vucinic, D.; Bingham, C.; Stewart, P. Primary and albedo solar energy sources for high altitude persistent air vehicle operation. *Energies* **2017**, *10*, 573. [CrossRef]
12. Taha, H. Urban climates and heat islands: Albedo, evapotranspiration, and anthropogenic heat. *Energy Build.* **1997**, *25*, 99–103. [CrossRef]
13. Hwang, R.L.; Lin, T.P.; Lin, F.Y. Evaluation and mapping of building overheating risk and air conditioning use due to the urban heat island effect. *J. Build. Eng.* **2020**, *32*, 101726. [CrossRef]
14. Jandaghian, Z.; Akbari, H. The effect of increasing surface albedo on urban climate and air quality: A detailed study for Sacramento, Houston, and Chicago. *Climate* **2018**, *6*, 19. [CrossRef]
15. Mohegh, A.; Levinson, R.; Taha, H.; Gilbert, H.; Zhang, J.; Li, Y.; Tang, T.; Ban-Weiss, G.A. Observational evidence of neighborhood scale reductions in air temperature associated with increases in roof albedo. *Climate* **2018**, *6*, 98. [CrossRef]
16. Tsoka, S.; Tsikaloudaki, K.; Theodosiou, T.; Bikas, D. Urban Warming and Cities' Microclimates: Investigation Methods and Mitigation Strategies—A Review. *Energies* **2020**, *13*, 1414. [CrossRef]
17. Wong, N.H.; Tan, C.L.; Kolokotsa, D.D.; Takebayashi, H. Greenery as a mitigation and adaptation strategy to urban heat. *Nat. Rev. Earth Environ.* **2021**, *2*, 166–181. [CrossRef]
18. Pasetto, M.; Baliello, A.; Pasquini, E.; Giacomello, G. High albedo pavement materials. In *Eco-Efficient Materials for Reducing Cooling Needs in Buildings and Construction*; Woodhead Publishing: Sawston, UK, 2021; pp. 15–32.
19. Fox, J.; Osmond, P.; Peters, A. The effect of building facades on outdoor microclimate—Reflectance recovery from terrestrial multispectral images using a robust empirical line method. *Climate* **2018**, *6*, 56. [CrossRef]
20. Aram, F.; Solgi, E.; Higueras García, E.; Mosavi, A.; Várkonyi-Kóczy, A. The cooling effect of large-scale urban parks on surrounding area thermal comfort. *Energies* **2019**, *12*, 3904. [CrossRef]
21. Malys, L.; Musy, M.; Inard, C. Direct and indirect impacts of vegetation on building comfort: A comparative study of lawns, green walls and green roofs. *Energies* **2016**, *9*, 32. [CrossRef]
22. Wang, J.; Ye, B.; Cui, Y.; He, X.; Yang, G. Spatial and Temporal Variations of Albedo on Nine Glaciers in Western China from 2000 to 2011. *Hydrol. Process.* **2014**, *28*, 3454–3465. [CrossRef]
23. Akbari, H.; Levinson, R.; Miller, W.; Berdahl, P. Cool colored roofs to save energy and improve air quality. In Proceedings of the 1st International Conference on Passive and Low Energy Cooling for the Built Environment, Athens, Greece, 17–24 May 2005.
24. Bozonnet, E.; Doya, M.; Allard, F. Cool roofs impact on building thermal response: A French case study. *Energy Build.* **2011**, *43*, 3006–3012. [CrossRef]

25. Meierhofer, A.; Bernsteiner, C.; Six, K.; Dietmaier, P. Improved prediction of shear stress and temperature distribution in the wheel-rail contact. In *Dynamics of Vehicles on Roads and Tracks Vol 2, Proceedings of the 25th International Symposium on Dynamics of Vehicles on Roads and Tracks (IAVSD 2017), Rockhampton, Australia, 14–18 August 2017*; CRC Press: Boca Raton, FL, USA, 2017; p. 621.
26. Calabrò, E.; Magazù, S. Correlation between increases of the annual global solar radiation and the ground albedo solar radiation due to desertification—A possible factor contributing to climatic change. *Climate* **2016**, *4*, 64. [CrossRef]
27. Liu, Q.; Wang, L.; Qu, Y.; Liu, N.; Liu, S.; Tang, H.; Liang, S. Preliminary evaluation of the long-term GLASS albedo product. *Int. J. Digit. Earth* **2013**, *6* (Suppl. S1), 69–95. [CrossRef]
28. Ceamanos, X.; Moparthy, S.; Carrer, D.; Seidel, F.C. Assessing the Potential of Geostationary Satellites for Aerosol Remote Sensing Based on Critical Surface Albedo. *Remote Sens.* **2019**, *11*, 2958. [CrossRef]
29. Levy, C.R.; Burakowski, E.; Richardson, A.D. Novel measurements of fine-scale albedo: Using a commercial quadcopter to measure radiation fluxes. *Remote Sens.* **2018**, *10*, 1303. [CrossRef]
30. Professor Crystal Schaaf's Lab. "MODIS Research" School for the Environment, University of Massachusetts Boston. Available online: https://www.umb.edu/spectralmass/terra_aqua_modis (accessed on 17 December 2023).
31. Roy, D.P.; Wulder, M.A.; Loveland, T.R.; Woodcock, C.E.; Allen, R.G.; Anderson, M.C.; Helder, D.; Irons, J.R.; Johnson, D.M.; Kennedy, R.; et al. Landsat-8: Science and product vision for terrestrial global change research. *Remote Sens. Environ.* **2014**, *145*, 154–172. [CrossRef]
32. Baldinelli, G.; Bonafoni, S.; Rotili, A. Albedo retrieval from multispectral Landsat 8 observation in urban environment: Algorithm validation by in situ measurements. *IEEE J. Sel. Top. Appl.* **2017**, *10*, 4504–4511. [CrossRef]
33. Fugazza, D.; Senese, A.; Azzoni, R.S.; Maugeri, M.; Maragno, D.; Diolaiuti, G.A. New Evidence of Glacier Darkening in the Ortles-Cevedale Group from Landsat Observations. *Glob. Planet. Chang.* **2019**, *178*, 35–45. [CrossRef]
34. Ma, Y.; He, T.; Liang, S.; Wen, J.; Gastellu-Etchegorry, J.P.; Chen, J.; Ding, A.; Feng, S. Landsat Snow-Free Surface Albedo Estimation Over Sloping Terrain: Algorithm Development and Evaluation. *IEEE Trans. Geosci. Remote Sens.* **2022**, *60*, 1–14. [CrossRef]
35. Naegeli, K.; Damm, A.; Huss, M.; Wulf, H.; Schaepman, M.; Hoelzle, M. Cross-Comparison of Albedo Products for Glacier Surfaces Derived from Airborne and Satellite (Sentinel-2 and Landsat 8) Optical Data. *Remote Sens.* **2017**, *9*, 110. [CrossRef]
36. Shuai, Y.; Masek, J.G.; Gao, F.; Schaaf, C.B. An algorithm for the retrieval of 30-m snow-free albedo from Landsat surface reflectance and MODIS BRDF. *Remote Sens. Environ.* **2011**, *115*, 2204–2216. [CrossRef]
37. Silva, B.B.D.; Braga, A.C.; Braga, C.C.; de Oliveira, L.M.; Montenegro, S.M.; Barbosa, B., Jr. Procedures for calculation of the albedo with OLI-Landsat 8 images: Application to the Brazilian semi-arid. *Rev. Bras. Eng. Agrícola Ambient.* **2016**, *20*, 3–8. [CrossRef]
38. Traversa, G.; Fugazza, D.; Senese, A.; Frezzotti, M. Landsat 8 OLI Broadband Albedo Validation in Antarctica and Greenland. *Remote Sens.* **2021**, *13*, 799. [CrossRef]
39. Wang, Y.; Bakker, F.; De Groot, R.; Wörtche, H. Effect of ecosystem services provided by urban green infrastructure on indoor environment: A literature review. *Build. Environ.* **2014**, *77*, 88–100. [CrossRef]
40. Liang, S.; Wang, J. Chapter 6—Broadband Albedo. In *Advanced Remote Sensing: Terrestrial Information Extraction and Applications*, 2nd ed.; Sparks, L., Janco, C., Eds.; Academic Press: Cambridge, MA, USA, 2020; pp. 193–250.
41. Markvart, T.; McEvoy, A.; Castañer, L. *Practical Handbook of Photovoltaics: Fundamentals and Applications*; Elsevier: Amsterdam, The Netherlands, 2020.
42. Qu, Y.; Liang, S.; Liu, Q.; He, T.; Liu, S.; Li, X. Mapping Surface Broadband Albedo from Satellite Observations: A Review of Literatures on Algorithms and Products. *Remote Sens.* **2015**, *7*, 990–1020. [CrossRef]
43. Ziar, H.; Sönmez, F.F.; Isabella, O.; Zeman, M. A comprehensive albedo model for solar energy applications: Geometric spectral albedo. *Appl. Energy* **2019**, *255*, 113867. [CrossRef]
44. Zheng, L.; Zhao, G.; Dong, J.; Ge, Q.; Tao, J.; Zhang, X.; Qi, Y.; Doughty, R.B.; Xiao, X. Spatial, temporal and spectral variations in albedo due to vegetation changes in China's grasslands. *ISPRS J. Photogramm. Remote Sens.* **2019**, *152*, 1–12. [CrossRef]
45. Landsat Science. Landsat 9. Available online: https://landsat.gsfc.nasa.gov/satellites/landsat-9/ (accessed on 17 December 2023).
46. Kasischke, E.S.; Goetz, S.J.; Kimball, J.S.; Mack, M.M. *The Arctic-Boreal Vulnerability Experiment (ABoVE): A Concise Plan for a NASA-Sponsored Field Campaign*; Final report on the VuRSAL/ABoVE scoping Study; NASA: Washinton, DC, USA, 2010.
47. Solvik, K.K.; Potter, S.; Erb, A.M.; Roman, M.; Schaaf, C.; Sun, Q.; Wang, Z.; Rogers, B.M. *ABOVE: MODIS-Derived Daily Mean Blue-Sky Albedo for Northern North America, 2000–2017*; ORNL DAAC: Oak Ridge, TN, USA, 2019. [CrossRef]
48. USGS. MCD43A1 v006. Available online: https://lpdaac.usgs.gov/products/mcd43a1v006/ (accessed on 17 December 2023).
49. Augustine, J.A.; DeLuisi, J.J.; Long, C.N. SURFRAD–A national surface radiation budget network for atmospheric research. *Bull. Am. Meteorol. Soc.* **2000**, *81*, 2341–2358. [CrossRef]
50. Global Monitoring Laboratory from NOAA. Available online: https://gml.noaa.gov/ (accessed on 17 December 2023).
51. Bastiaanssen, W.G.M.; Menenti, M.; Feddes, R.A.; Holtslag, A.A.M. A Remote Sensing Surface Energy Balance Algorithm for Land. *J. Hydrol.* **1998**, *213*, 198–212. [CrossRef]
52. Chen, T.S.; Ohring, G. On the relationship between clear-sky planetary and surfae albedos. *J. Atmos. Sci.* **1984**, *41*, 156–158. [CrossRef]

53. Yoder, R.E.; Odhiambo, L.O.; Wright, W.C. Effects of vapor-pressure deficit and net-irradiance calculation methods on accuracy of standardized Penman-Monteith equation in a humid climate. *J. Irrig. Drain. Eng.* **2005**, *131*, 228–237. [CrossRef]
54. Allen, R.G.; Tasumi, M.; Trezza, R.; Waters, R.; Bastiaanssen, W. Sebal (surface energy balance algorithms for land). *Adv. Train. Users Man.–Ida. Implement.* **2002**, *1*, 97.
55. Liang, S.; Strahler, A.H.; Walthall, C. Retrieval of land surface albedo from satellite observations: A simulation study. *J. Appl. Meteorol. Climatol.* **1999**, *38*, 712–725. [CrossRef]
56. Jiménez-Muñoz, J.C.; Sobrino, J.A.; Skoković, D.; Mattar, C.; Cristóbal, J. Land surface temperature retrieval methods from Landsat-8 thermal infrared sensor data. *IEEE Geosci. Remote Sens. Lett.* **2014**, *11*, 1840–1843. [CrossRef]
57. Rouse, J.W. *Monitoring the Vernal Advancement of Retrogradation of Natural Vegetation*; type III; final report; NASA/GSFC: Greenbelt, MD, USA, 1974; p. 371.
58. Sabziparvar, A.; Mousavi, M.; Torabzadeh, H. Variability Of Surface Albedo, Vegetation Cover In Hyrcanian Forests Of Iran. In Proceedings of the 2nd International Symposium on Natural Hazards and Disaster Management, Sakarya University Culture and Congress Center 2018, Sakarya, Turkey, 4–6 May 2018.
59. Sánchez-Zapero, J.; Camacho, F.; Martínez-Sánchez, E.; Lacaze, R.; Carrer, D.; Pinault, F.; Benhadj, I.; Muñoz-Sabater, J. Quality Assessment of PROBA-V Surface Albedo V1 for the Continuity of the Copernicus Climate Change Service. *Remote Sens.* **2020**, *12*, 2596. [CrossRef]
60. Wang, Z.; Schaaf, C.B.; Strahler, A.H.; Chopping, M.J.; Román, M.O.; Shuai, Y.; Woodcock, C.E.; Hollinger, D.Y.; Fitzjarrald, D.R. Evaluation of MODIS Albedo Product (MCD43A) over Grassland, Agriculture and Forest Surface Types during Dormant and Snow-Covered Periods. *Remote Sens. Environ.* **2014**, *140*, 60–77. [CrossRef]
61. Global Monitoring Laboratory. SURFRAD Site Information. Available online: https://gml.noaa.gov/grad/surfrad/sitepage.html (accessed on 17 December 2023).
62. Hashim, H.; Abd Latif, Z.; Adnan, N.A. Urban vegetation classification with NDVI thresold value method with very high resolution (VHR) PLEIADES Imagery. *Int. Arch. Photogramm. Remote Sens. Spat. Inf. Sci.-ISPRS Arch.* **2019**, *XLII–4/W16*, 237–240. [CrossRef]
63. Zhan, W.; Chen, Y.; Zhou, J.; Wang, J.; Liu, W.; Voogt, J.; Zhu, X.; Quan, J.; Li, J. Disaggregation of remotely sensed land surface temperature: Literature survey, taxonomy, issues, and caveats. *Remote Sens. Environ.* **2013**, *131*, 119–139. [CrossRef]
64. Marion, B. Measured and satellite-derived albedo data for estimating bifacial photovoltaic system performance. *Sol. Energy* **2021**, *215*, 321–327. [CrossRef]

Disclaimer/Publisher's Note: The statements, opinions and data contained in all publications are solely those of the individual author(s) and contributor(s) and not of MDPI and/or the editor(s). MDPI and/or the editor(s) disclaim responsibility for any injury to people or property resulting from any ideas, methods, instructions or products referred to in the content.